DIRECT NUMERICAL SIMULATION OF AN IMPINGING JET

Yongmann M. Chung[1]
[1]Department of Engineering, University of Warwick
Coventry CV4 7AL, U.K.
Y.M.Chung@Warwick.ac.uk

Kai H. Luo[2]**, Neil D. Sandham**[3]**, and John J. R. Williams**[2]
[2]Department of Engineering, Queen Mary, University of London
London E1 4NS, U.K.

[3]School of Engineering Sciences, University of Southampton
Southampton SO17 1BJ, U.K.

ABSTRACT

Numerical simulations of unsteady heat transfer of an impinging jet are performed. The correlation between the flow structure and the impingement heat transfer is examined. It was found that the local heat transfer was very unsteady in nature and correlated closely with the flow structure. Detailed analysis of the instantaneous flow field and the heat transfer characteristics shows that strong unsteadiness of the impingement heat transfer is mainly caused by the primary vortices emanating from the nozzle of the jet. Unsteady separation caused by the primary vortices also plays an important role in the unsteady impingement heat transfer.

INTRODUCTION

Impinging jets have been encountered in a variety of practical engineering applications. For example, the dynamics of impinging jets are very important in developing vertical take-off and landing (VTOL) aircraft. Impinging jets have also been used as an effective method to enhance or suppress the heat transfer. In the metal sheet production process, impinging jets have been used to quench hot metal sheets from the furnace. A survey of configurations of jet impingement heat transfer studies is available in Viskanta (1993). A great number of studies have dealt with the heat transfer enhancement due to impinging jets and extensive reviews have been provided by Martin (1977), Jambunathan et al. (1992), and Viskanta (1993). The effects on the impingement heat transfer of several parameters such as the jet Reynolds number, nozzle-to-plate distance, nozzle geometry, and roughness of the impinging wall have been investigated.

It is known from flow visualisation studies that impinging jet flows are very unsteady and complicated (Popiel and Trass, 1991). The unsteadiness of the flow originates inherently from the primary vortices emanating from the nozzle of the jet caused by the shear layer instability of a Kelvin-Helmholtz type. The primary vortices dominate the impinging jet flow as they approach the wall. Large-scale coherent structures are found to play a dominant role in momentum transfer of the impinging jet (Didden and Ho, 1985; Olsson and Fuchs, 1998). After the primary vortices deflect from the wall, they convect along the impinging wall, and unsteady separation may occur. The time dependent separation of the wall jet part of an impinging jet was investigated experimentally by Didden and Ho (1985).

Due to the highly unsteady flow characteristics, the impingement heat transfer is also strongly time dependent. However, most studies to date have focused on the time-mean heat transfer and the unsteady characteristics of the impingement heat transfer are not fully yet understood and only a few studies are available in the literature (Özdemir and Whitelay, 1992). The unsteady heat transfer in an excited circular impinging jet was investigated by Liu and Sullivan (1996). They found that enhancement and reduction of the local heat transfer were related to the changes in the flow structures when an impinging jet was forced at different frequencies. It is important, therefore, to understand the unsteady heat transfer characteristics associated with the coherent flow

structures.

In the present study, direct numerical simulations of an unsteady impinging jet at low Reynolds numbers are performed to study the unsteady impingement heat transfer. The unsteady compressible Navier-Stokes equations are solved in this study. A high-order finite difference method is used with accurate non-reflecting boundary conditions. The instantaneous flow fields of an impinging jet are examined to investigate the effect of the coherent vortical structures on the unsteady impingement heat transfer.

NUMERICAL METHOD

Governing equations

For a compressible viscous flow, the governing equations (the unsteady continuity equation, Navier-Stokes equations, energy equation and scalar transport equation) can be written as follows using the conservative variables $(\rho, \rho u_i, E_T, \rho f)$ (Luo and Sandham, 1997):

$$\frac{\partial \rho}{\partial t} + \frac{\partial \rho u_i}{\partial x_i} = 0, \quad (1)$$

$$\frac{\partial \rho u_i}{\partial t} + \frac{\partial \rho u_i u_j}{\partial x_j} = -\frac{\partial p}{\partial x_j}\delta_{ij} + \frac{\partial \tau_{ij}}{\partial x_j}, \quad (2)$$

$$\frac{\partial E_t}{\partial t} + \frac{\partial E_t u_i}{\partial x_i} = -\frac{\partial p u_i}{\partial x_i} - \frac{\partial q_i}{\partial x_i} + \frac{\partial u_j \tau_{ij}}{\partial x_i}, \quad (3)$$

$$\frac{\partial \rho f}{\partial t} + \frac{\partial \rho u_j f}{\partial x_j} = \frac{1}{ReSc}\frac{\partial}{\partial x_i}\left(\mu \frac{\partial f}{\partial x_i}\right) \quad (4)$$

where ρ is the density, u_i are the velocity components for x_i directions, p is the thermodynamic pressure, τ_{ij} is the shear stress tensor, q_i is the heat flux vector, and f is the scalar variable. E_T is the total energy density (thermal + kinetic), defined by

$$E_T = \rho\left(e + \frac{1}{2}u_i u_i\right), \quad (5)$$

where, e is the internal energy per unit mass $(\rho e = p/(\gamma - 1))$.

Constitutive relations for the shear stress tensor τ_{ij} and the heat flux vector q_i are given by

$$\tau_{ij} = \frac{\mu}{Re}\left(2S_{ij} - \frac{2}{3}\frac{\partial u_k}{\partial x_k}\delta_{ij}\right), \quad (6)$$

$$q_i = \frac{-\mu}{(\gamma - 1)M^2 PrRe}\frac{\partial T}{\partial x_i}, \quad (7)$$

where the viscosity μ is assumed to follow a power law, $\mu = T^{0.76}$ for air. The strain rate S_{ij} is defined by

$$S_{ij} = \frac{1}{2}\left(\frac{\partial u_i}{\partial x_j} + \frac{\partial u_j}{\partial x_i}\right). \quad (8)$$

Here, Re is the Reynolds number, M is the Mach number, Pr is the Prandtl number, Sc is the Schmidt number, and γ is the ratio of the specific heat. The physical constants used in the simulation are $Pr = 1.0, Sc = 1.0$, and $\gamma = 1.4$.

Boundary conditions

The mean velocity profile at the inflow is a top-hat profile with smooth edges. A hyperbolic tangent profile is used:

$$U = \frac{U_c + U_a}{2} + \frac{U_c - U_a}{2}\left(1 + \tanh\left(\frac{x}{2\theta}\right)\right), \quad (9)$$

where θ is the inflow momentum thickness and U_c is the jet centre-line velocity. The co-flow velocity U_a is chosen to be zero in this study.

A variety of non-reflecting boundary conditions are used in the simulation. At the inflow boundary, the non-reflecting boundary condition of Poinsot and Lele (1992) is implemented, allowing the density to change in time. At the wall, the non-reflecting boundary condition of Poinsot and Lele (1992) is implemented together with the no-slip conditions. At the lateral exit, Thompson's (1987) non-reflecting boundary condition is applied in parallel to the buffer layer. The constant temperature boundary condition is imposed at the impinging wall.

Numerical techniques

For spatial discretisation, a sixth-order finite-difference compact scheme of Lele (1992) is used in all directions. The spatially discretised governing equations are advanced in time explicitly with a low storage third-order Runge-Kutta method. After both flow and thermal field have reached a quasi-steady state, the averages over time were taken for several periods. For the definition of the period, refer to the next section.

RESULTS AND DISCUSSION

In the present simulation, all the flow variables are non-dimensionalised by the jet centre-line velocity U_c and the jet width D, and the resulting Reynolds number is $Re = U_c D/\nu$. The ratio of the jet width to the inflow momentum thickness is $D/\theta = 20$. The ratio of the jet temperature to the impinging wall temperature is

1.25. A Cartesian coordinate system centred at the stagnation point on the impinging wall is used: x is the direction parallel to the impinging wall, and y is the negative jet direction (see Fig. 1). The corresponding lateral and axial velocities are u and v. The computational domain size of interest is L_x, and L_y. Simulations with two values for the nozzle-to-plate distance ($L_y/D = 4$ and 10) were performed. It is known that the extent of the potential core is 4–8 jet widths for slot nozzles (Livingood and Hrycak, 1973). $L_y/D = 10$ is chosen to analyse the fully developed jet impingement case and $L_y/D = 4$ is for the under-developed jet impingement case. Grid refinement is performed until more grid points do not cause any significant differences in the result. Effects of computational time step were investigated by successively halving the time step until stable solutions were obtained. Simulations were performed at four Reynolds numbers, $Re = 300$, 500, 1000, and 3000. The numerical parameters used in the present study are summarised in Table 1.

Unsteady impinging jet

To investigate the unsteady impingement heat transfer, the flow field of $Re = 500$ is analysed in detail (Case 2). Figure 1 shows the temperature and vorticity contour lines at three time instants together with the definition of the relevant coordinates. The jet comes from the top and the impinging wall is located at $y = 0$. In this simulation, no forcing is imposed at the inflow and the jet develops in varicose (symmetric) mode near the jet nozzle. The primary vortices emanating from the jet shear layer are clearly seen, which is the characteristic of the unsteady jet flow. As the flow is deflected from the impinging wall, a wall jet is developed. The wall jet separates due to the interaction with the primary vortices and the impinging wall and secondary vortices are formed. The interaction of the primary vortices with the wall shear layer gives rise to unsteady vortical motions.

The primary vortices close to the impinging wall are denoted by PV in the figure, where NV represents the next primary vortices emanating from the jet shear layer. The secondary vortices are indicated by SV in the lower part of Fig. 1. As can be seen in Fig. 1 (a), the primary vortex PV locates very close to the wall at P1. The proximity of the strong primary vortex results in a thin shear layer and consequently a thin thermal boundary layer along

Case	Re	M	L_x	L_y	$Nx \times Ny$
Case 1	300	0.3	10	10	256×256
Case 2	500	0.3	10	10	300×300
Case 3	1000	0.3	10	10	384×384
Case 4	3000	0.3	10	10	256×256
Case 5	300	0.3	8	4	256×256
Case 6	500	0.3	8	4	256×256
Case 7	1000	0.3	8	4	256×256
Case 8	3000	0.3	8	4	256×256
Case 9	500	0.1	10	10	300×300
Case 10	500	0.2	10	10	300×300
Case 12	500	0.4	10	10	300×300
Case 13	500	0.5	10	10	300×300
Case 14	500	0.6	10	10	300×300
Case 15	500	0.7	10	10	300×300

Table 1: Numerical parameters of impinging jet simulations.

the wall.

As the primary vortex PV moves downstream, the temperature near the stagnation point decreases due to the thickening of the thermal boundary layer. The vorticity contour lines during the temperature-decreasing phase (see Fig. 3) are displayed in Fig. 1 (b). As the primary vortex PV progresses downstream, the location of the primary vortices, y_v, increases slightly again indicating a thickening of the thermal boundary layer downstream along the impinging wall (Didden and Ho, 1985). This feature is responsible for the decrease in the local minimum Nusselt number during the temperature-decreasing phase (see Fig. 3 (a)). The passage of the primary vortex PV is associated with a vorticity maximum at the impinging wall. The interaction of the primary vortex PV with the shear layer results in a secondary vortex near the wall at the later stage of the temperature-decreasing phase at P3. The primary and secondary vortices are counter-rotating.

As the primary vortex PV moves further downstream with the new primary vortex NV not yet affecting the dynamics near the impinging wall directly, the stagnation Nusselt number keeps decreasing. Figure 1 (c) shows the temperature and vorticity contour lines at P4 corresponding to a local minimum of the stagnation Nusselt number. The formation of the secondary vortex SV is clearly seen at $x = 3$. The secondary vortex SV is detached from the wall and results in unsteady separation. The unsteady separation region moves downstream together with the primary vortex PV. Upstream of the unsteady separation region, the instantaneous Nusselt number has a local minimum, as seen in Fig. 3. A secondary maximum instantaneous Nusselt number was observed in the separation region.

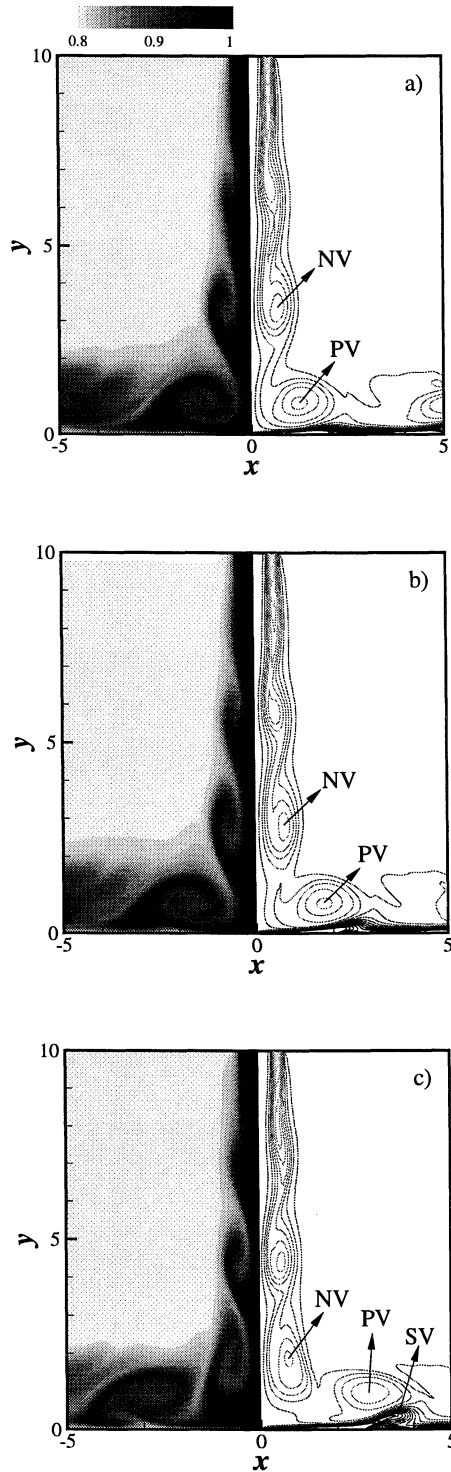As the new primary vortex NV approaches

Figure 1: Temperature (left) and vorticity (right) contour lines at several time instants for $Re = 500$. at a) P1, b) P2, and c) P4.

towards the wall, the stagnation Nusselt number begins to increase again. The primary vortex PV is located far from the stagnation point and has little influence on the heat transfer near the stagnation region. The influence from the new primary vortex NV is, however, increasing as it approaches the wall.

	t	Nu_{stag}	x_v	y_v	ω_v
P1	34.26	17.33	1.25	0.83	1.92
P2	35.59	16.05	1.78	0.79	1.90
P3	36.93	13.56	2.34	0.87	1.82
P4	38.25	13.01	2.82	0.98	1.78
P5	39.56	14.47	3.28	1.10	1.75
P6	40.85	17.22	3.67	1.15	1.73

Table 2: Data at several time instants marked (Case 2). x_v and y_v are the location of the primary vortex (PV), and ω_v is the strength of the primary vortex.

The location and strength of the primary vortex PV are summarised in Table 2. The location of the primary vortex shows a characteristic V-shape (Didden and Ho, 1985). The strength of the vortex is weakened during the period due to the viscosity but the decrease is only 10 % of the strength. It is found that the modulation of the instantaneous Nusselt number is attributed to the dynamics of the primary vortices emanating from the jet shear layer as well as the strength of the vortices.

Unsteady impingement heat transfer

Temperatures very close to the wall are monitored to understand the characteristics of the unsteady heat transfer of an impinging jet. Figure 2 shows the time history of the temperature at $y \approx 0.02$ at several locations along the wall for $L_y/D = 10$. The temperature variation is directly related to the Nusselt number, defined as

$$Nu = \frac{hD}{k}, \qquad (10)$$

where h is the heat transfer coefficient and k is the thermal conductivity of the fluid.

As the first primary vortices emanating from the jet shear layer approach the wall, they cause a rapid change in temperature near the stagnation point. In Fig. 2, a sudden increase in temperature at $x = 0$ is seen at about $t = 16$ for all three Reynolds numbers. After the primary vortices impinge the wall, the jet flow changes the flow direction and the primary vortices progress downstream along the wall. The temperature increase caused by the moving primary vortices becomes smaller as the flow goes downstream further due to the continuous mixing with the surrounding fluid. After an early transient period $(0 < t < 25)$, the temperatures show unsteady and oscillating behaviour. The fluctuations in the temperature increase with Reynolds number and at $Re = 500$ the oscillating behaviour of the temperature is clearly seen at all measuring locations. This is due to the direct influence of the coherent vortical structure of the impinging

274

Figure 3: Instantaneous Nusselt number along the impinging wall for $Re = 500$ (Case 2). a) temperature-decreasing phase ($34.66 \leq t \leq 38.06$), and b) increasing phase ($38.06 \leq t \leq 41.38$). Time increment between each line is 0.326.
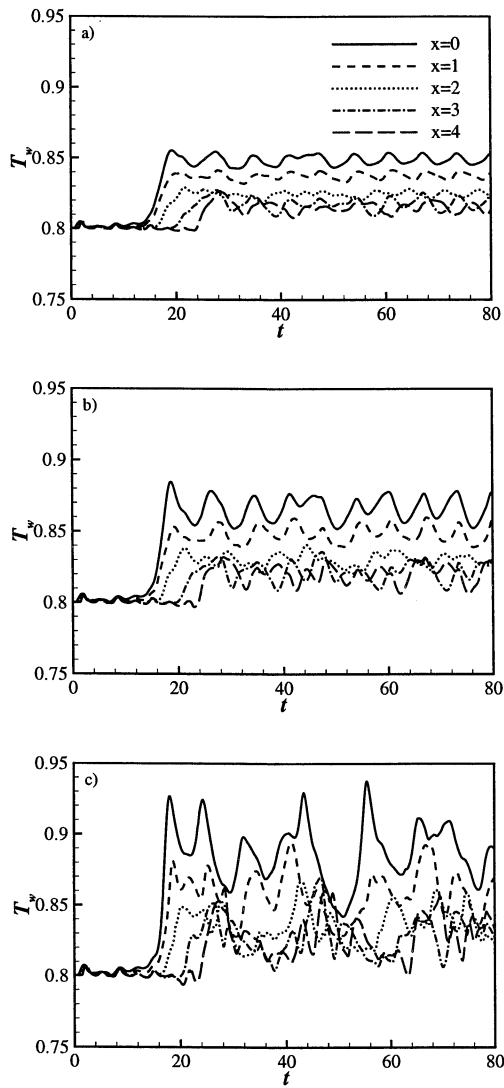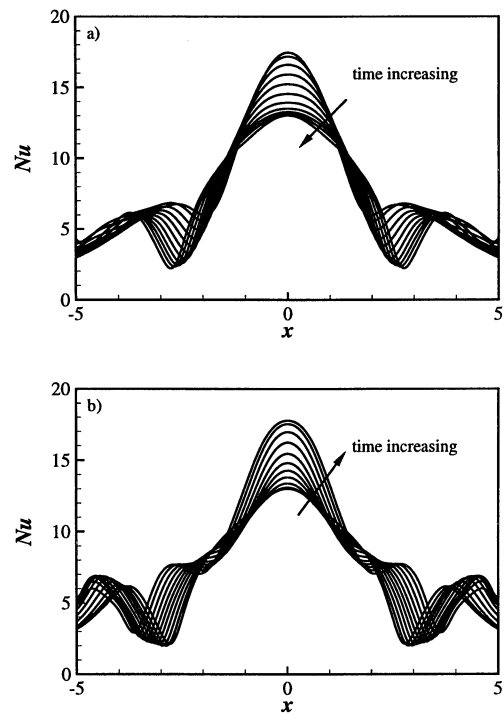
Figure 2: Time history of temperature (at $y \approx 0.02$) at several locations near the wall for $L_y/D = 10$. a) $Re = 300$, b) 500, and c) 1000.

jet shown in Fig. 1. The unsteady temperature distributions show that the heat transfer characteristics at $Re = 500$ are sufficiently coherent and repeatable, although the behaviour is not perfectly periodic. It is found that in the present study the dominant frequency corresponds to a Strouhal number of $St \approx 0.2$, based on U_c and D. This value falls within the range of other experimental (Didden and Ho, 1985; Ho and Huerre, 1984) and numerical (Olsson and Fuchs, 1998; Hoffmann and Benocci, 1994) results.

Some effects of the Reynolds number are found in Fig. 2. For a lower Reynolds number ($Re = 300$), the unsteadiness of the temperature data is reduced substantially, mainly due to the weakness of the vortex formation in the jet shear layer. It is not surprising because

at a low Reynolds number the viscous effects usually weaken the shear layer instability. The vortex formation is not completely suppressed but the weak vortices make the interaction with the impinging wall much weaker. As the Reynolds number increases, the temperature data become irregular at $Re = 1000$, although the shedding is still discernible.

To understand the unsteady heat transfer characteristics, the instantaneous Nusselt number distributions during a typical *period* are analysed. Since the temperature variation does not have a perfect periodicity as shown in Fig. 2, the time duration between two consecutive local maxima of the stagnation Nusselt number is considered as a *period* in this analysis. The half of the period between a local maximum to a local minimum is referred to as the temperature-decreasing phase and the other half between a local minimum to the next local maximum is referred to as the temperature-increasing phase. Figure 3 shows the instantaneous Nusselt number distributions along the impinging wall during one typical period for the three Reynolds numbers, respectively. The beginning and the end of the period is indicated in the caption of each figure.

The heat transfer coefficient generally decreases as the distance from the stagnation

point increases. The maximum heat transfer is found at the stagnation point at all time instants as expected, although the absolute value is modulating substantially. During the temperature-decreasing phase shown in Fig. 3 (a), the location for the local minimum moves downstream and the magnitude of the local minimum decreases in time. This is because the thermal boundary layer becomes thicker for $2 \leq x \leq 3$ during this phase. During the temperature-increasing phase shown in Fig. 3 (b), the magnitude of the local minimum is almost the same as the location itself moves downstream. As the Reynolds number increases, the instantaneous Nusselt number distributions become more irregular.

CONCLUDING REMARKS

Unsteady heat transfer characteristics of an impinging jet flow have been studied numerically. The instantaneous Nusselt number has very strong fluctuations and the unsteadiness increases with Reynolds number. Detailed analysis of the instantaneous flow field and heat transfer characteristics has been performed. It is found that the unsteady heat transfer characteristics are strongly correlated with the vortex dynamics of the jet flow. The oscillating behaviour of the impingement heat transfer is caused directly by the primary vortices moving towards the impinging wall. Unsteady separation also plays an important role in the impingement heat transfer. Unsteady separation induces a secondary maximum and a local minimum of the instantaneous heat transfer along the impinging wall. The instantaneous Nusselt number had a local minimum upstream of the unsteady separation region due to the thickened thermal boundary layer. A secondary maximum in the instantaneous Nusselt number was observed in the separation region. The secondary maximum is attributed to the engulfing motion around the secondary vortex.

ACKNOWLEDGEMENTS

REFERENCES

Didden, N., and Ho, C. M., 1985, "Unsteady separation in a boundary layer produced by an impinging jet," *Journal of Fluid Mechanics*, Vol. **160**, pp. 235–256.

Hoffmann, G., and Benocci, C., 1994, "Numerical simulation of spatially-developing planar jets," In *Application of direct and large eddy simulation to transition and turbulence*, AGARD-CP-551, pp. 26-1-26-6.

Jambunathan, K., Lai, E., Moss, M. A., and Button, B. L., 1992, "A review of heat transfer data for single circular jet impingement," *International Journal of Heat and Fluid Flow*, Vol. **13**, pp. 106–115.

Lele, S. K., 1992, "Compact finite difference schemes with spectral-like resolution," *Journal of Computational Physics*, Vol. **103**, pp. 16–42.

Liu, T., and Sullivan, J. P., 1996, "Heat transfer and flow structure in a excited circular impinging jet," *International Journal of Heat and Mass Transfer*, Vol. **39**, No. 17, pp. 3695–3706.

Livingood, N. B., and Hrycak, P., 1973, "Impingement heat transfer from turbulent air stream jets to flat plates - a literature survey," NASA TM X-2778, Lewis Research Center, USA.

Luo, K. H., and Sandham, N. D., 1997, "Direct numerical simulation of supersonic jet flow," *Journal of Engineering Mathematics*, Vol. **32**, pp. 121–142.

Martin, H., 1977, "Heat and mass transfer between impinging gas jets and solid surfaces," *Advances in Heat Transfer*, Vol. **13**, pp. 1–60.

Olsson, M., and Fuchs, L, 1998, "Large eddy simulations of a forced semiconfined circular impinging jet," *Physics of Fluids*, Vol. **10**, No. 2, pp. 476–486.

Poinsot, T. J., and Lele, S. K., 1992, "Boundary conditions for direct simulations of compressible viscous flows," *Journal of Computational Physics*, Vol. **101**, pp. 104–129.

Popiel, C. O., and Trass, O., 1991, "Visualization of a free and impinging round jet," *Experimental Thermal and Fluid Science*, Vol. **4**, pp. 253–264.

Thompson, K. W., 1987, "Time dependent boundary conditions for hyperbolic systems," *Journal of Computational Physics*, Vol. **68**, pp. 1–24.

Viskanta, R., 1993, "Heat transfer to impinging isothermal gas and flame jets," *Experimental Thermal and Fluid Science*, Vol. **6**, pp. 111–134.